

IC-FNM 2016

Effect of pyrolysis process parameters on electrical, physical, chemical and electro-chemical properties of SU-8-derived carbon structures fabricated using the C-MEMS process

Bidhan Pramanick^a, Matias Vazquez-Pinon^a, Alejandro Torres-Castro^b,
Sergio O. Martinez-Chapa^{a, *}, and Marc Madou^{a, c, †}

^a School of Engineering and Sciences, Tecnológico de Monterrey, Monterrey, N.L., 64849, Mexico

^b Mechanical and Electrical Engineering School, Universidad Autónoma de Nuevo León, San Nicolás de los Garza, N.L., 66455, Mexico

^c Department of Mechanical and Aerospace Engineering, University of California, Irvine, CA, 92697, USA

Abstract

Pyrolysis is the process to thermally decompose an organic material into its carbon backbone in an oxygen-free environment. This process is used in the Carbon-MEMS fabrication technology to carbonize micro-structures patterned on a substrate. The properties of the resulting carbon material are dependent on either the carbon precursor or the pyrolysis conditions. In this work, SU-8 photoresist was used as the carbon precursor to study the effects of three pyrolysis parameters: 1) maximum pyrolysis temperature (600°C, 700°C, 800°C, and 900°C), 2) temperature ramp rate (2.5°C/min, 5°C/min, 10°C/min, and 20°C/min), and 3) nitrogen flow rate (3l/min, 4.5l/min, 6l/min, and 7.5l/min). To study the effect of the maximum temperature, the temperature ramp rate and nitrogen flow rate were kept constant to 5°C/min and 6l/min respectively. For the temperature ramp rate experiments, we kept the maximum pyrolysis temperature and nitrogen flow rate constant to 900°C and 6l/min respectively. For the nitrogen flow rate study, the maximum pyrolysis temperature and temperature ramp rate were kept constant to 900°C and 5°C/min respectively. We found that no polymer structures persisted under the following conditions: 900°C maximum pyrolysis temperature, 5°C/min temperature ramp rate, and 3l/min nitrogen flow rate. Under these conditions the nitrogen flow rate is not high enough to keep the furnace environment (approximate volume of the furnace tube we used is 6l) entirely inert; in the pyrolysis process, even a small amount of oxygen destroys the intended C-MEMS. All the carbon samples were characterized using 4-point probe measurement for electrical resistivity; confocal microscopy for pore size determination; Raman spectroscopy, electron diffraction x-ray spectroscopy (EDX), and x-ray photoelectron spectroscopy (XPS) for chemical characterization.

* Corresponding author. Tel.: +52-818-328-4095; fax: +52-818-328-4095.

E-mail address: smart@itesm.mx

† Corresponding author. Tel.: +1-949-824-6585; fax: +1-949-824-8585.

E-mail address: mmadou@uci.edu

Furthermore, the samples were electrochemically characterized using cyclic voltammetry in a 1mM $K_4Fe(CN)_6$ and 0.5M KCl solution. The characterization results suggest that samples prepared under the following conditions - 900°C maximum pyrolysis temperature, 5°C/min temperature ramp rate, and 6l/min nitrogen flow rate, exhibit the best electrical, physical, chemical and electrochemical properties among the other conditions used.

© 2017 Elsevier Ltd. All rights reserved.

Selection and/or Peer-review under responsibility of International Conference on Functional Nano-Materials, 2016.

Keywords: carbon-MEMS; pyrolysis; carbon electrodes; electrochemical sensor; fabrication; photolithography;

1. Introduction

Over the last 15 years, carbon microelectromechanical systems (C-MEMS) have gained widespread interest due to the low cost, reliability and simplicity of their fabrication that result in a wide variety of 2D and 3D carbon patterns [1-4]. The C-MEMS process has been utilized to fabricate carbon materials in many applications including electrochemical sensing [5], substrate for molecular electronics [6], electrodes for batteries [7-9], fuel cells [10], dielectrophoretic separators [11, 12], and capacitors [13-15], scaffolds [16], nanogaps [17], hot nanowires for local CVD [5], molds for bulk metallic glasses [18], and gas sensors [19, 20]. Generally, C-MEMS process comprises two steps: photolithography and pyrolysis. Briefly, a one-step photolithography process is used to pattern a photo-sensitive polymer and the patterned structures are converted into carbon using thermochemical decomposition (also known as pyrolysis).

During pyrolysis, the organic precursor material is heated in an inert atmosphere to temperatures above 600°C. This step defines the material composition of the structures, which in turn defines the physico-chemical properties of the resulting carbon shapes (such as electrical and thermal conductivities, chemical reactivity, and mechanical stiffness, among others) [21-25]. Several parameters of the pyrolysis process can be adjusted to fine-tune the physico-chemical properties of the fabricated carbon devices. For example, flow of nitrogen (N_2), argon (Ar), or mixtures of gases such as forming gas (95% N_2 and 5% H_2) are commonly used to create an inert pyrolysis atmosphere, with each atmosphere yielding carbon structures with different properties. More critical parameters are the maximum pyrolysis temperature, heating ramp rates, and gas flow rate. Therefore, a complete investigation of the effect of these process parameters on the C-MEMS physico-chemical properties is of utmost importance to meet the requirements of the C-MEMS application at hand.

The pyrolysis process is used to convert a polymer precursor into pure carbon. At the high temperature, all the non-carbon atoms break away from the pyrolyzing polymer matrix and depending on the process settings, the escaping gasses may result in porous or dense carbon structures. The pyrolysis process needs to be carried out in an inert environment; even a very small amount of oxygen can burn out the structures and make them unusable. The source of O_2 may be an air leakage into the pyrolysis chamber, oxygen back diffusion or it may even come from the sample itself. Here we discuss three pyrolysis parameters that need to be investigated to obtain quality carbon structures: 1) the maximum pyrolysis temperature, 2) temperature ramp rate, and 3) gas flow rate (N_2 in this case). SU-8 structures were pyrolyzed for four different values of each of these parameters and the samples were characterized for each parameter setting to investigate the effect of the pyrolysis condition.

2. Experimental

2.1. Fabrication of SU-8 structures: photolithography

Conventional photolithography process was used for the fabrication of the SU-8 polymeric structures [7]. As the substrate for the carbon structures, a 4-inch silicon wafer with a 1 μm thermally-oxidized SiO_2 layer (NOEL Technologies, Campbell, CA, USA) was used. SU-8 2007 negative photoresist (PR) (MicroChem Corp. Westborough, MA, USA) was spin-coated on the substrate at 3000 rpm for 30 seconds, to a final layer thickness of 7 μm , and soft-baked on a hotplate for 2.5 minutes at 95°C to evaporate the PR solvents and achieve an even distribution of the layer on the substrate. The photoresist was then exposed to UV radiation through a thin film

photomask to a total energy of 120 mJ/cm², and then baked again for 3.5 minutes at 95°C to crosslink the exposed patterns. Finally, the unexposed regions were dissolved in SU-8 PR developer solution by dipping the samples for 2 minutes.

2.2. Fabrication of carbon structures: pyrolysis

Twelve patterned SU-8 samples were divided in three groups of four to study the effect of pyrolysis parameters. All samples were pyrolyzed in a pressurized furnace, (PEO 601, ATV Technologie GmbH, Germany) using the following temperature profile: (I) the temperature was increased from room temperature to 300°C at a determined temperature ramp rate, and maintained at that temperature for 60 min for thermal stabilization; (II) then, the temperature was increased from 300°C to the maximum pyrolysis temperature using the same temperature ramp rate and kept constant for 60 min; (III) Finally, the furnace was cooled down to room temperature at 10°C/min.

To study of the effect of the maximum pyrolysis temperature on the material properties, four different temperatures were used: 600°C, 700°C, 800°C and 900°C; while the temperature ramp rate was fixed to 5°C/min and the nitrogen flow rate to 6l/min for all four pyrolysis runs. Then, to analyse the effect of the temperature ramp rate, the maximum pyrolysis temperature was fixed to 900°C and the nitrogen flow rate to 6l/min, while four temperature ramp rates were studied: 2.5°C/min, 5°C/min, 10°C/min and 20°C/min. Finally, to study the effect of the nitrogen flow rate, the samples were pyrolyzed under four different nitrogen flow rate conditions: 3l/min, 5l/min, 6l/min and 7.5l/min, using a maximum pyrolysis temperature and temperature ramp rate constant at 900°C and 5°C, respectively.

2.3. Characterization

Optical images of the surface of the samples were obtained by confocal microscopy (Axio CSM 700, Carl Zeiss, DE) to subsequently analyse the pore size distribution using ImageJ software (National Institute of Health, Bethesda, MD, USA). The pyrolyzed carbon structures were electrically characterized using the 4-point probe method for resistivity measurements (Agilent 34401A, Agilent Technologies, Santa Clara, CA, USA). The crystallinity variation of the materials was examined with Raman spectroscopy (inVia Qontor, Renishaw plc, UK) using a 514 nm Ar laser source. The chemical composition of the samples was investigated using energy-dispersive X-ray spectroscopy (TESCAN VEGA 3, Czech Republic) with a 20 kV accelerating voltage. Finally, an X-ray photoelectron spectroscopy (Thermo Scientific, USA) analysis was carried out to quantify the elements present on the surface of the structures.

2.4. Electrochemical characterization

The carbon structures were mounted as the working electrode in an electrochemical cell containing 1mM K₄Fe(CN)₆ and 0.5M KCl diluted in DI water. A platinum wire was used as the counter electrode and commercially available Ag/AgCl electrode was used as reference electrode. Cyclic voltammetry experiments were conducted with a potentiostat (CH Instrument 760E, TX, USA) by applying a linear potential sweep from -200 mV to 600 mV between reference and working electrodes on a scan rate of 50 mV/s.

3. Results and discussion

C-MEMS fabrication process and a schematic diagram of the pyrolyzed structure used for this study are shown in Figure 1. Here, two electrode pads of 3 mm × 3 mm area are connected through a 5 mm-long and 1 mm-wide strip. One pad is assigned for electrical connection by means of soldering and the other for electrochemical sensing. In this section, we present the characterization results of only eleven pyrolyzed structures, since the polymer structure pyrolyzed at 3l/min nitrogen flow rate did not withstand the process. We investigated the reason and present it in the following section.

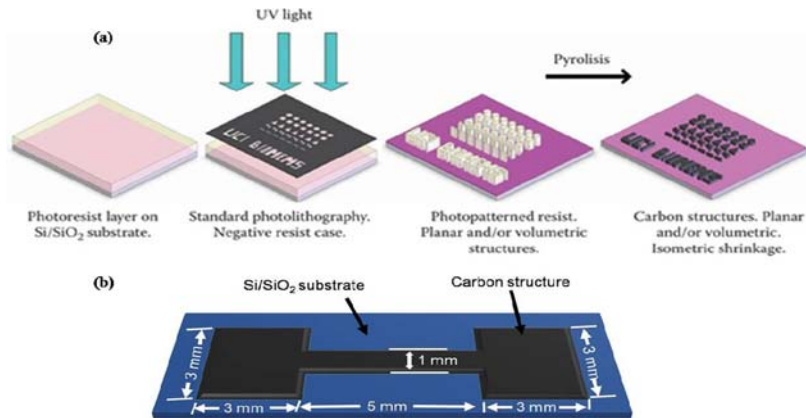


Fig. 1. (a) An illustration of one type of C-MEMS: photolithographic patterning of a polymer precursor (SU-8 photo resist) and pyrolysis [22]; (b) Schematic of the pyrolyzed structure.

3.1. Effect of maximum pyrolysis temperature

We present the optical images of pyrolyzed structure surfaces in Figure 2a-d, and the pore size distribution is presented in Figure 2e. It was noticed that as the pyrolysis temperature increases, the maximum pore size of the material decreases.

In this case, the inert environment inside the furnace tube is ensured due to the high nitrogen flow rate. At the temperature of 600 °C, polymer structure loses maximum numbers of non-carbon atoms as degassing, causing gas bubble flow inside the polymer structure which creates pores bigger in size. These pores are annealed out with the increase of temperature, 700 °C, 800 °C, 900 °C, and become smaller

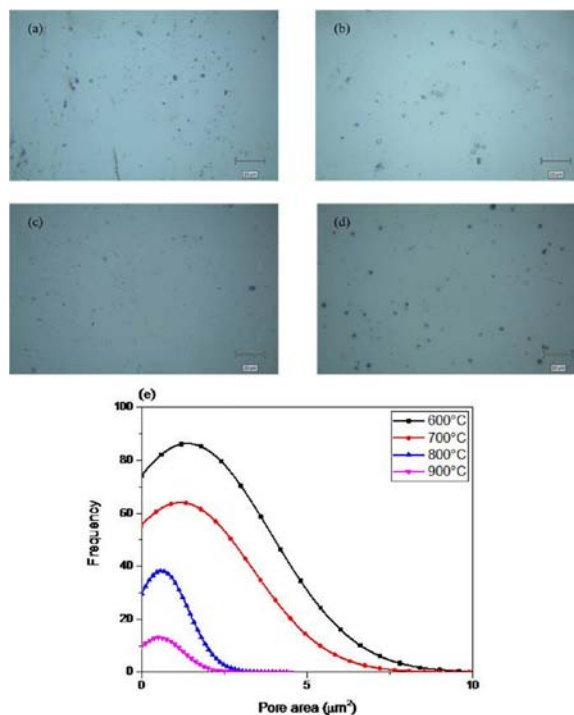


Fig. 2. Optical images of the pyrolyzed structure surface prepared at (a) 600°C, (b) 700°C, (c) 800°C, and (d) 900°C. Scale bar is 20μm. (e) Pore size distribution for different maximum pyrolysis temperature.

The bond of non-carbon atoms with carbon breaks in increasing rate with the increase of temperature, therefore, the structure becomes more conductive with the increase of temperature. With this, the atomic percentage of carbon increases. The resistivity of the pyrolyzed structures as a function of the maximum pyrolyzed temperature is presented in Figure 3. The resistivity of the material, ρ , decreases one order of magnitude from values in the range of $10^4 \Omega$ to $10^3 \Omega$, when moving from 600°C to 700°C . This decrease tendency is even clearer at 800°C , where ρ is decreased by two orders of magnitude, compared to 700°C , reaching values of $10^2 \Omega$. The further temperature increase in this case was not highly significant in terms of resistivity.

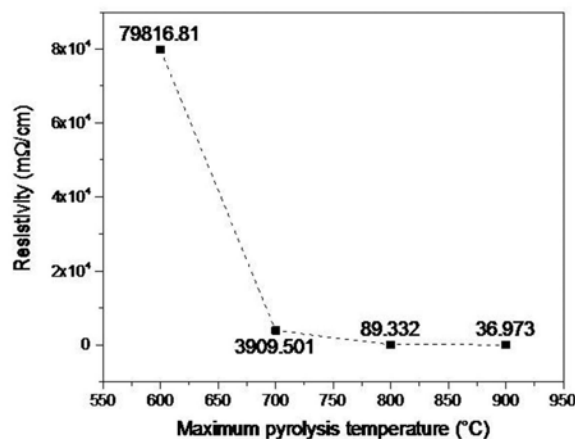


Fig. 3. Resistivity changes with maximum pyrolysis temperatures.

The variation in the atomic percentage of the elements present in the structure, obtained by EDX, is shown in Table 1. Silicon was detected because of the substrate used, Si/SiO₂, which was also exposed to the electron beam while performing EDX due to the penetration of the beam into the sample. It can be seen from Table 1 that the atomic percentage of all the elements is constant with the temperature variation from 600°C throughout 800°C . We also obtained similar results of increased atomic percentage of carbon at 900°C , yielding a higher amount of C-C bonds, which considerable reduces the electron beam energy; therefore, the substrate is less exposed to the beam and, in consequence, the atomic percentage of silicon is significantly reduced. This reduction also causes a small increment in oxygen atomic percentage.

Table 1. Atomic percentage of the elements present in the pyrolyzed structure.

Elements	Atomic percentage of elements at different pyrolysis temperatures			
	600°C	700°C	800°C	900°C
Carbon	86.30	86.16	86.62	89.84
Oxygen	3.17	2.57	2.58	3.78
Silicon	10.53	11.27	10.80	6.38

The precise information of elements present on the surface of the structures was obtained using XPS. The element peak intensities as a function of the maximum pyrolysis temperature are shown in Figure 4a. In this case, only carbon and oxygen atoms were found in the analysis. The variation of atomic percentages of C_{1s} and O_{1s} with pyrolysis temperature is shown in Figure 4b. The atomic percentage of carbon and the atomic percentage ratio of carbon and oxygen, C:O, both are increased with the pyrolysis temperature. Higher value of the C:O ratio signifies the higher carbon atomic percentage and lesser oxygen. The ratios were calculated to be 2.43, 50.54, 54.48 and 60.73 for 600°C , 700°C , 800°C and 900°C , respectively.

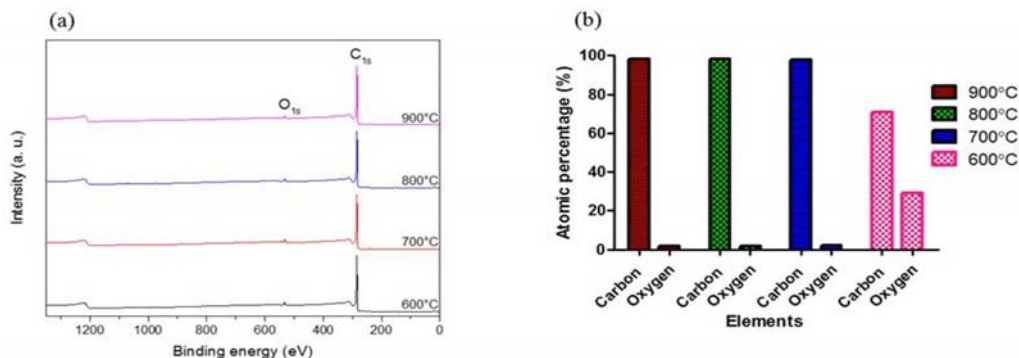


Fig. 4. XPS analysis results (a) elements intensity with binding energy, and (b) atomic percentage variation of the elements at different pyrolysis temperatures.

Raman spectroscopy results of the fabricated structures for the pyrolysis temperature effect study are shown in Figure 5a and 5b, showing the first-order and second-order scattering, respectively. The first-order region, up to 1800 cm^{-1} , exhibits two dominant bands: disordered band or D-band, at around 1395 cm^{-1} , and ordered band or G-band, at around 1605 cm^{-1} [26]. As the temperature increases, both bands decrease their half-widths and show a small frequency shift. The intensity ratio of the two dominant bands (ID/IG) is taken as a measure of the structural disorder. In this case, ID/IG decreases with the increase of pyrolysis temperature from 700°C to 900°C, indicating an increase in crystallinity. For the samples prepared at a 600°C, the G-band intensity was considerably higher than the D band, but G-peak broadening is also observed, which is an indicative of bond length scatter and disorder at the molecular level in the form of strained bonds[27]. Some of these strains are relieved with the increasing temperature through contraction, expansion, or coalescence of C-C bonds at the atomic scale [28].

The second-order Raman spectra, above 2300 cm^{-1} , are even more sensitive to disorder [26]. For samples prepared at a 600°C, the band measured at around 2775 cm^{-1} corresponds to the allowed second harmonics of the vibrations observed in the first-order spectra. The remaining two bands, at around 2920 cm^{-1} and at around 2360 cm^{-1} are forbidden combinations made active by atomic disorder [26]. These bands are virtually disappeared from the spectra of better-ordered samples prepared at higher temperatures (from 700°C to 900°C), which contain larger crystallites.

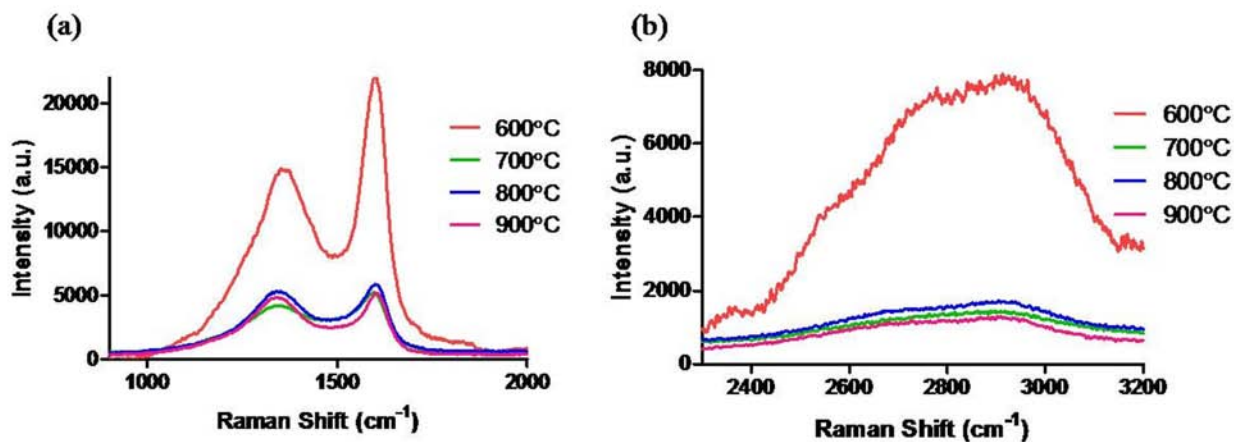


Fig. 5. Raman spectroscopy for different pyrolysis temperatures. (a) first-order and (b) second-order scattering.

The pyrolyzed samples were mounted for the electrochemical sensing experiments and the recorded cyclic voltammograms are shown in Figure 6. The oxidation and reduction peaks were found to be at 188 mV and 321 mV, respectively for the sample prepared at 900°C. The structures pyrolyzed below 900°C are more electrochemically resistive to perform oxidation/reduction, therefore, we did not obtain any peaks for those samples.

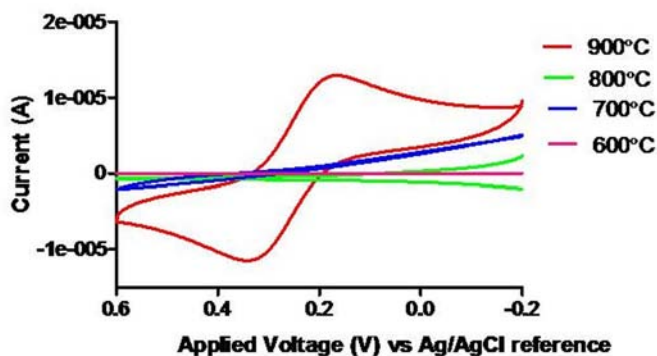


Fig. 6. Cyclic voltammogram recorded for different pyrolysis temperatures.

3.2. Effect of temperature ramp rate

The optical images of pyrolyzed structure surfaces for the analysis of temperature ramp rate variation are presented in Figure 7a-d and the pore size distribution is presented in Figure 7e. The maximum pore size decreases with the increase of the temperature ramp rate from 2.5°C/min to 5°C/min and increases for higher rates: 10°C/min and 20°C/min.

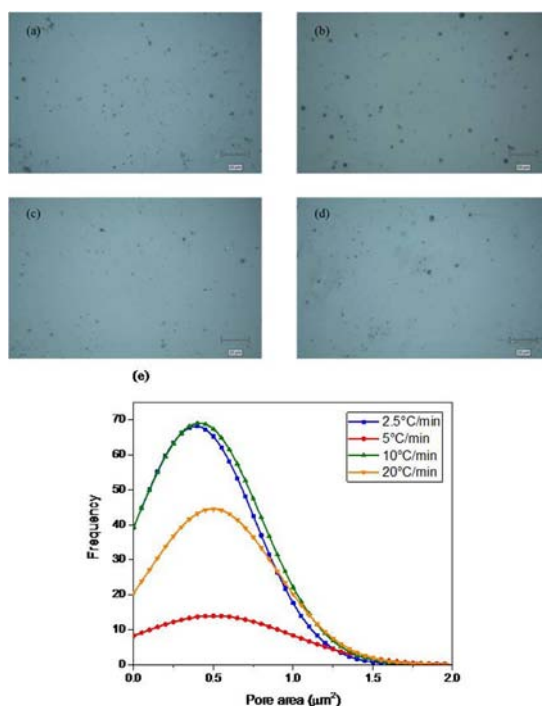


Fig. 7. Optical images of the pyrolyzed structure surface prepared at (a) 2.5°C/min, (b) 5°C/min, (c) 10°C/min, and (d) 20°C/min. Scale bar is 20μm. (e) Pore size distribution for different temperature ramp rate.

Two factors are responsible of the pore formation in this case: oxidation process and pyrolysis. For the highest rates (10°C/min and 20°C/min ramp rates), the pores are formed due to degassing and could not anneal out. For the slow flow rates (2.5°C/min to 5°C/min), the non-carbon atoms loss occurs on a slower rate, therefore, the oxygen, present in the polymer structure itself or the impurity of the nitrogen flow, could oxidize the structure rather breaking out from polymer chain.

The resistivity of the pyrolyzed structures with temperature ramp rate is presented in Figure 8. Resistivity decreases 7.5% with the increase of temperature ramp rate, from 2.5°C/min to 5°C/min and then, it increases 2.25% and 0.7% for 10°C/min and 20°C/min respectively.

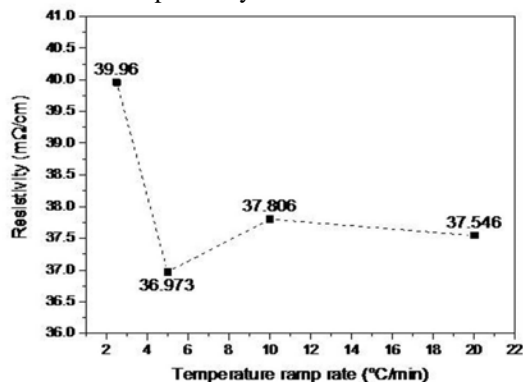


Fig. 8. Resistivity changes with different temperature ramp rates.

The changes on the atomic percentage of elements in the structure, is shown in Table 2. It can be seen from the table that the atomic percentage of carbon increases when the temperature ramp rate is increased from 2.5°C/min to 5°C/min and it decreases with further increment in temperature ramp rate.

Table 2. Atomic percentage of the elements present in the pyrolyzed structure.

Elements	Atomic percentage of elements at different temperature ramp rates			
	2.5°C/min	5°C/min	10°C/min	20°C/min
Carbon	82.55	89.84	84.42	85.01
Oxygen	4.20	3.78	3.29	2.73
Silicon	13.25	6.38	12.29	12.26

The element peak intensity, obtained from XPS analysis is shown in Figure 9a, and the variation of atomic percentages of carbon and oxygen with temperature ramp rate is shown in Figure 9b. The atomic percentage of carbon and the C:O ratio, both are increased with the increase of temperature ramp rate from 2.5°C/min to 5°C/min and both are decreased for the increase of temperature ramp rate to 10°C/min. Both the values are increased for further increment from 10°C/min to 20°C/min. The C:O ratios were calculated to be 16.83, 60.73, 34.54, and 46.17 for 2.5°C/min, 5°C/min, 10°C/min and 20°C/min, respectively.

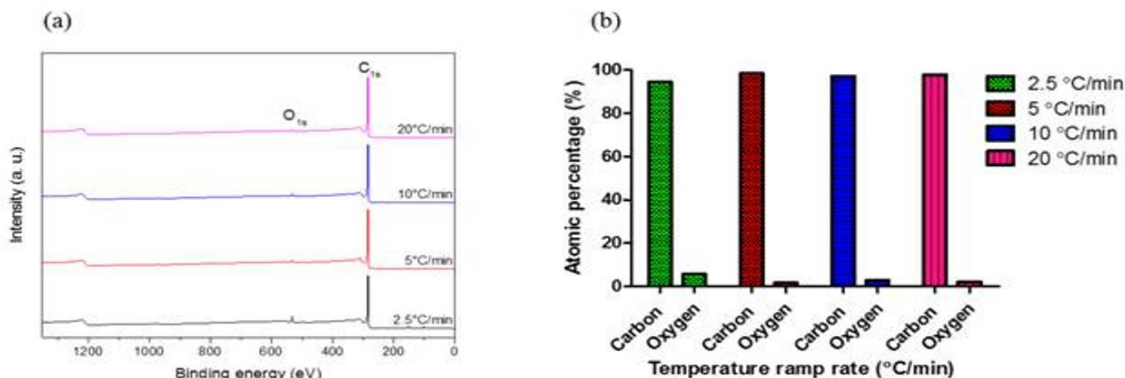


Fig. 9. XPS analysis results of (a) elements intensity with binding energy, and (b) atomic percentage variation of the elements at different temperature ramp rates.

Raman spectroscopy analysis results of the fabricated structures for the pyrolysis temperature ramp rate effect study are shown in Figure 10a and b, showing the first-order and second-order scattering respectively. For the first-order region, D- and G-bands are measured at around 1395 cm^{-1} and 1605 cm^{-1} , respectively. In this case, peak broadening of disordered band is also observed for slow ramp rate, 2.5°C/min , and fast ramp rates, 10°C/min and 20°C/min , compared to 5°C/min . So as, I_D/I_G decreases with the increase of temperature ramp rate from 2.5°C/min to 5°C/min , and increases with a further increase of the ramp rate. Similar second-order Raman spectra were also measured for all the samples prepared at different temperature ramp rates. The band was measured at around 2775 cm^{-1} and 2920 cm^{-1} for all the samples. With this information, we assume that the shape of these bands is more dependent on the pyrolysis temperatures [26].

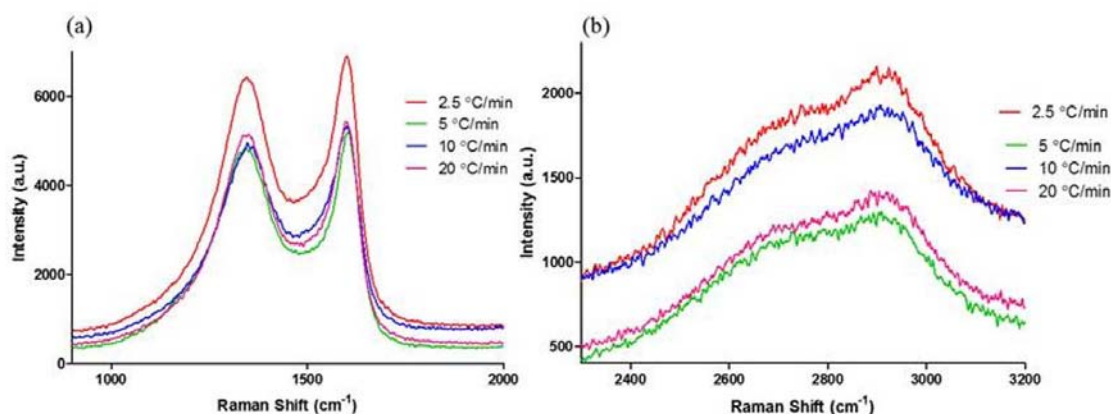


Fig. 10. Raman spectroscopy for different temperature ramp rates. (a) first-order and (b) second-order scattering.

The cyclic voltammograms for the pyrolyzed samples at different temperature ramp rates are shown in Figure 11. The variation of measured oxidation and reduction peaks with temperature ramp rates is presented in Table 3. The measured oxidation and reduction currents for 20°C/min temperature ramp rate is very small compared to other processes. This is because of the fast structural change which induces defects in the structure.

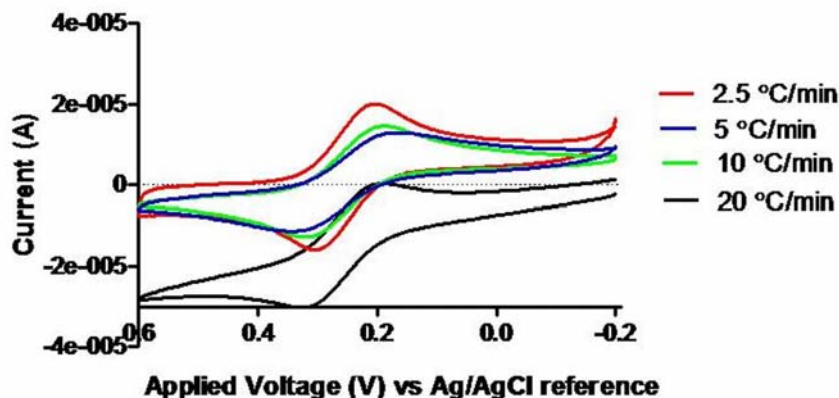


Fig. 11. Cyclic voltammogram recorded for different temperature ramp rates.

Table 3. The variation of oxidation and reduction peaks with temperature ramp rates

Temperature ramp rate (°C/min)	Oxidation peak at voltage (mV)	Reduction peak at voltage (mV)
2.5	204	302
5	188	321
10	190	312
20	198	322

3.3. Effect of nitrogen flow rate

The optical images of pyrolyzed structure surfaces for nitrogen flow rate variation are presented in Figure 12a-d, and the pore size distribution is presented in Figure 12e. The maximum pore size decreases with the increase of nitrogen flow rate from 4.5 l/min to 6 l/min. At 4.5 l/min flow rate, inert environment inside the furnace tube is not well established, therefore, the pore size is dependent on the incorporation of oxygen. Maximum pore size also increases with the increase of nitrogen flow rate from 6 l/min to 7.5 l/min. In this case, the interaction of inert gas and the sample surface is hindered for high flow rate and the foreign species, mainly oxygen from the polymer structure, are adsorbed at the surface rather leaving the structure. This adsorption enhances pore size by oxidizing the structure.

The resistivity of the pyrolyzed structures with temperature ramp rate is presented in Figure 13. Resistivity decreases 92.6% with the increase of nitrogen flow rate, from 4.5 l/min to 6 l/min and it increases 48.48% with the increase of nitrogen flow rate, from 6 l/min to 7.5 l/min. The changes of the atomic percentage of the elements present in the structure are shown in Table 4. It can be seen from the table that the atomic percentage of carbon increases when the nitrogen flow rate is increased from 4.5 l/min to 6 l/min and it decreases with further increment to 7.5 l/min.

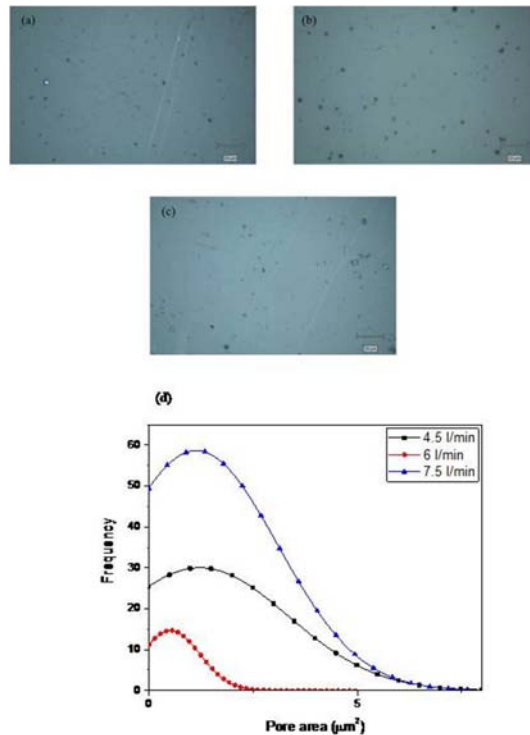


Fig. 12. Optical images of the pyrolyzed structure surface prepared at (a) 4.5 l/min, (b) 6 l/min, and (c) 7.5 l/min nitrogen flow rate. Scale bar is 20 μm. (d) Pore size distribution for different nitrogen flow rates.

Table 4. Atomic percentage of the elements present in the pyrolyzed structure.

Elements	Atomic percentage of elements at different nitrogen flow rates		
	4.5l/min	6l/min	7.5l/min
Carbon	60.56	89.84	81.98
Oxygen	23.08	3.78	4.71
Silicon	16.36	6.38	13.31

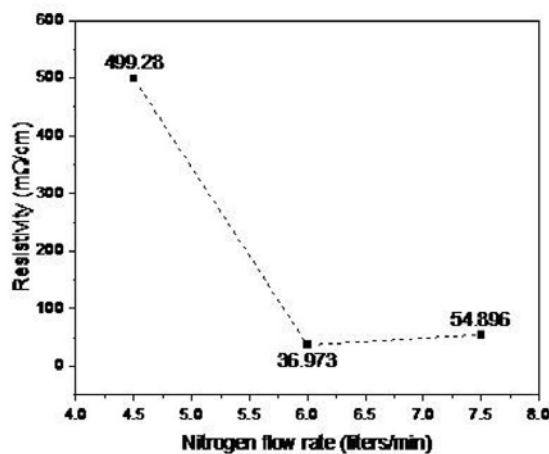


Fig. 13. Resistivity changes with nitrogen flow rates.

The element peak intensity is shown in Figure 14a, and the variation of atomic percentages of carbon and oxygen with temperature ramp rate is shown in Figure 14b. The atomic percentage of carbon and the C:O ratio, both increase when the nitrogen flow rate is increased from 4.5l/min to 6l/min and decrease with further increment to 7.5 l/min. The C: O ratios were calculated to be 35.36, 60.73, and 32.56 for 4.5l/min, 6l/min, and 7.5l/min, respectively.

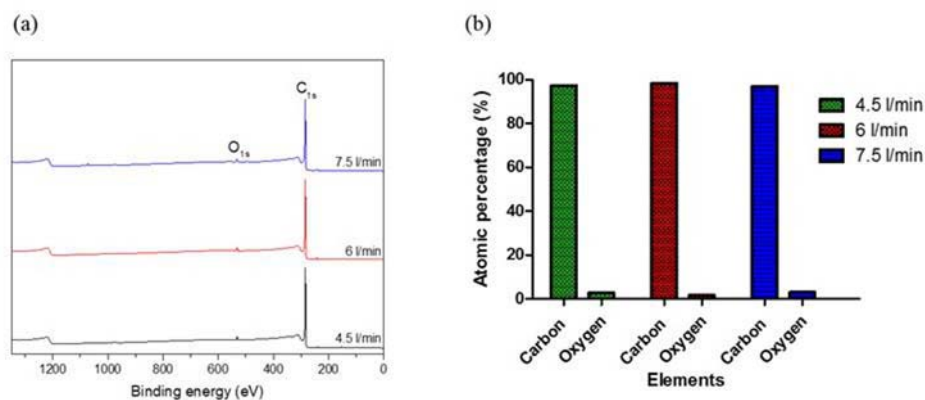


Fig. 14. XPS analysis results of (a) elements intensity with binding energy, and (b) atomic percentage variation of the elements at different nitrogen flow rates.

Raman spectroscopy analysis results of the fabricated structures for the nitrogen flow rate effect study are shown in Figure 15a and 15b, showing the first-order and second-order scattering respectively. For the first-order region, D-band and G-band are measured at around 1395 cm^{-1} and at around 1605 cm^{-1} respectively, like other

experimental studies. Peak broadening is also observed for lower and higher nitrogen flow rates, than 6l/min. Therefore, I_D/I_G decreases with the increase of nitrogen flow rate from 4.5l/min to 6l/min and increases with the increase of nitrogen flow rate from 6l/min to 7.5l/min. In this case, the second-order Raman spectra were measured for all of the samples prepared at different nitrogen flow rates and the bands measured at around 2775 cm^{-1} and at around 2920 cm^{-1} for all the samples. It can be seen from the Figure 15b that sample prepared at 6l/min nitrogen flow rate is more ordered compared to others.

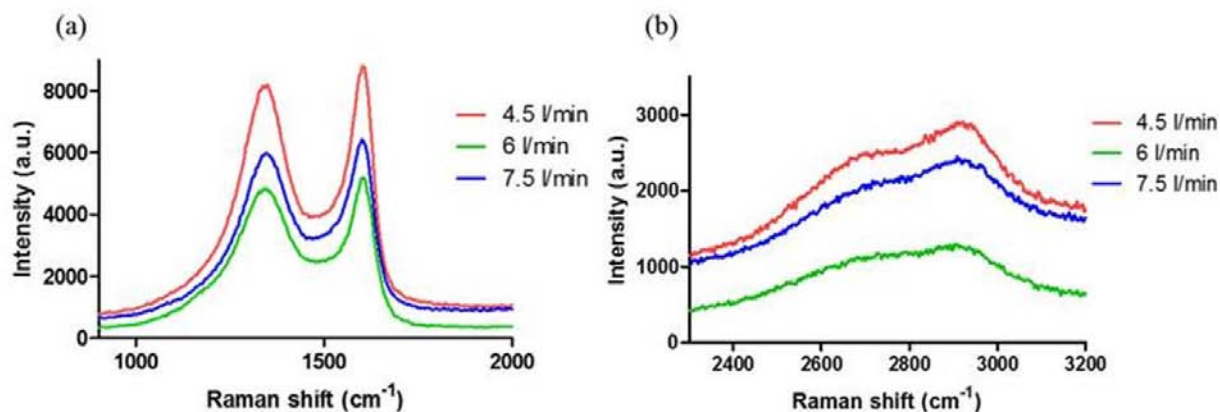


Fig. 15. Raman spectroscopy for different nitrogen flow rates. (a) first-order and (b) second-order scattering.

The recorded cyclic voltammograms for the pyrolyzed samples of different nitrogen flow rates were shown in Figure 16. The oxidation and reduction peaks were found to be at 188 mV and 321 mV respectively for the sample prepared at 6l/min nitrogen flow rate; 188 mV and 365 mV respectively for the sample prepared at 7.5l/min nitrogen flow rate. The measured currents at oxidation are also same for both the samples, but the current at reduction is very small for 7.5l/min compared to 6l/min nitrogen flow rate. This is because the structure prepared at 7.5l/min nitrogen flowrate is more resistive due more oxygen present in it. For the sample prepared at 4.5l/min nitrogen flow rate, no proper peaks of oxidation and reduction are found.

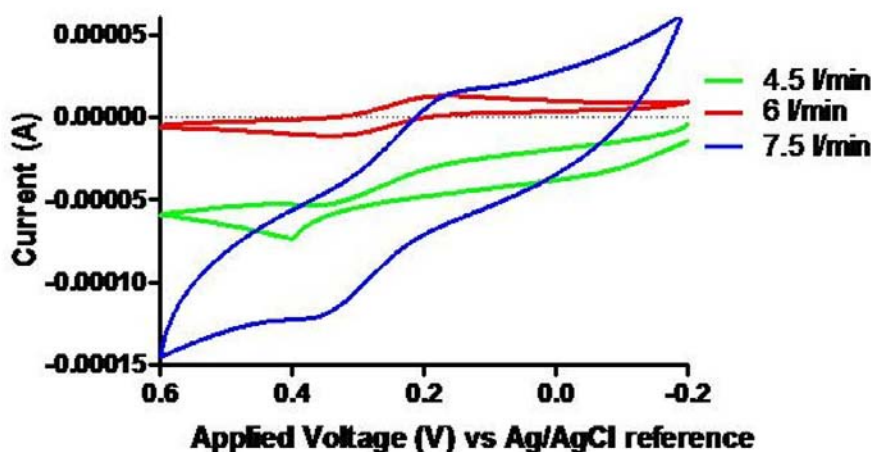


Fig. 16. Cyclic voltammogram recorded for different nitrogen flow rates.

4. Conclusions

We fabricated carbon structures by the C-MEMS process, and investigated the effect of three pyrolysis process parameters: maximum pyrolysis temperature, temperature ramp rate and nitrogen flow rate, on the carbon structures. In this work, we chose four different values for each of the parameters and pyrolyzed the patterned SU-8 polymer structures accordingly. The structures prepared at lowest nitrogen flow rate, 3l/min, were washed away from the substrate as the complete inertness of the furnace tube environment was not ensured. A complete inert environment must be ensured in the furnace during the pyrolysis, or a small incorporation of oxygen may yield unusable structures. We characterized eleven of the structures using confocal microscopy, 4-probe measurement, Raman spectroscopy, EDX and XPS. The chemical reactivity and physical changes of the polymer structures depend on the temperature ramp rate as well as on the nitrogen flow rate. Temperature ramp rate directly influences the chemical reaction rate and the bi-products generated due to this reaction should be taken away from the structure surface at an optimized rate, or the physical changes will be affected. To achieve a good quality carbon structure, the maximum pyrolysis temperature is the most important parameter and we found the maximum temperature of 900°C among other used conditions to be best for electrochemical sensing application. 1mM $K_4Fe(CN)_6$ electrolyte in 0.5M KCl solution was used for the test and the best performed structure was pyrolyzed using following parameters: 900°C maximum pyrolysis temperature, 5°C/min temperature ramp rate and 6l/min nitrogen flow rate.

The nitrogen flow rate is dependent on the furnace tube volume. Therefore, the required nitrogen flow rate will be different for different volume furnaces. We considered the flow volume (/min) of 0.5 (3l), 0.75 (4.5l), 1 (6l) and 1.5 (7.5l) times the furnace volume and concluded that the optimized flow volume (/min) is equal with the volume of the furnace. The effect of the other two parameters should be same for any furnace. Our experimental study provides the information about the effect of three important pyrolysis parameters, therefore, one can choose appropriate parameters for particular application.

Acknowledgements

The authors would like to acknowledge the financial support from Conacyt in Mexico (grant no. CB-2014-1-241458 and postdoctoral fellowship no. 232499). This work was also financially supported by the Sensors and Devices Group of Tecnológico de Monterrey. Raman spectroscopy was performed at Water Center Facility, Tecnológico de Monterrey.

References

- [1] O.J.A. Schueller, S.T. Brittain, and G.M. Whitesides. *Advanced Materials* 9 (1997) 477–480.
- [2] O.J.A. Schueller, S.T. Brittain, C. Marzolin, G.M. Whitesides, *Chem. Mater.* 9 (1997) 1399–1406.
- [3] A. Singh, J. Jayaram, M. Madou, S. Akbar, *J. Electrochem. Soc.* 149 (2002), E78–E83.
- [4] M. Madou, V.H. Perez-Gonzalez, B. Pramanick, *Carbon: The Next Silicon? Book 1 - Fundamentals*, Momentum Press, New York, 2016.
- [5] S. Sharma, *Microstructural Tuning of Glassy Carbon for Electrical and Electrochemical Sensor Applications*, PhD Thesis, University of California Irvine, (2013).
- [6] G.S. Bisht, G. Canton, A. Mirsepassi, L. Kulinsky, S. Oh, D. Dunn-Rankin, M.J. Madou, *Nano Lett.* 11 (2011) 1831–1837.
- [7] C. Wang, G. Jia, L.H. Taherabadi, M.J. Madou, *J. Microelectromechanical Syst.* 14 (2005) 348–358.
- [8] C. Wang, L. Taherabadi, G. Jia, M. Madou, Y. Yeh, B. Dunn, *Electrochemical and Solid-State Letters* 7 (2004), A435–A438.
- [9] C. Wang, M.J. Madou, *Biosens. Bioelectron.* 20 (2005) 2181–2187.
- [10] A. Smirnova, X. Dong, H. Hara, A. Vasiliev, N. Sammes, *International Journal of Hydrogen Energy* 30 (2005) 149–58.
- [11] R. Martinez-Duarte, P. Renaud, M.J. Madou, *Electrophoresis.* 32 (2011) 2385–2392.
- [12] R.R. Kamath, M.J. Madou, *Anal. Chem.* 86 (2014) 2963–2971.
- [13] C. Kim, Y.-O. Choi, W.-J. Lee, K.-S. Yang, *Electrochimica Acta.* 50 (2004) 883–887.
- [14] L. Zhang, H. Liu, M. Wang, L. Chen, *Carbon* 45 (2007.) 1439–1445.
- [15] M. Madou, V.H. Perez-Gonzalez, B. Pramanick, *Carbon: The Next Silicon? Book 2 - Applications*, Momentum Press, New York, 2016.
- [16] L. Amato, A. Heiskanen, C. Caviglia, F. Shah, K. Zor, M. Skolimowski, M. Madou, L. Gammelgaard, R. Hansen, E.G. Seiz, M. Ramos, T. Moreno, A. Martínez-Serrano, S.S. Keller, J. Emnéus, *Advanced Functional Materials* 24 (2014) 7042–52.

- [17] A. Salazar, B.C. Benítez, B. Pramanick, S. Martinez-Chapa, M. Madou, 11th International Conference on Micromanufacturing (2016) UCI, CA, USA.
- [18] J. Schroers, G. Kumar, M. Madou, R. Martinez-Duarte, Carbon Molds for Use in the Fabrication of Bulk Metallic Glass Parts and Molds. Google Patents (2010).
- [19] S. Sharma, M. Madou, Philosophical Transactions of the Royal Society A: Mathematical, Physical and Engineering Sciences 370 (2011) 2448–2473.
- [20] C. Wang, L. Yin, L. Zhang, D. Xiang, R. Gao, Sensors 10 (2010) 2088–2106.
- [21] R. Martinez-Duarte, Micromachines, 5 (2014) 766–782.
- [22] M.J. Madou, From MEMS to Bio-MEMS and Bio-NEMS: Manufacturing Techniques and Applications, 3rd ed. edition, CRC Press, (2011).
- [23] B.Y. Park, L. Taherabadi, C. Wang, J. Zoval, M.J. Madou, J. Electrochem. Soc. 152 (2005) J136–J143.
- [24] A. Mardegan, R. Kamath, S. Sharma, P. Scopece, P. Ugo, M. Madou, J. Electrochem. Soc. 160 (2013) B132–B137.
- [25] S. Ranganathan, R. McCreery, S.M. Majji, M. Madou, J. Electrochem. Soc. 147 (2000) 277–282.
- [26] L. Soukup, I. Gregora, L. Jastrabik, A. Konakova, Materials Science and Engineering B11(1992) 355–357.
- [27] P. K. Chu, L. Li, Materials Chemistry and Physics 96 (2006) 253–277.